



A guidable nonlocal low-rank approximation model for hyperspectral image denoising

Yong Chen ^a, Juan Zhang ^a, Jinshan Zeng ^{a,*}, Wenzhen Lai ^a, Xinfeng Gui ^a, Tai-Xiang Jiang ^b

^a School of Computer and Information Engineering, Jiangxi Normal University, Nanchang, China

^b School of Economic Information Engineering, Southwestern University of Finance and Economics, Chengdu, China

ARTICLE INFO

Keywords:

Hyperspectral image denoising
Low-rank subspace representation
Nonlocal self-similarity
Guided image

ABSTRACT

Hyperspectral image (HSI) denoising is an essential preprocessing step for improving HSI applications. Recently, subspace-based nonlocal low-rank approximation (SNLR) methods have shown their superiority. However, most of these methods ignore such a potentially important phenomenon, that is, real HSIs contain many high signal-to-noise ratio bands (HSNRBs), and thus result in the underutilization of information. In this paper, we propose a new method called Subspace-based Guided Nonlocal Low-Rank Approximation (SGNLR) for HSI denoising. Our method takes advantage of the abundant spatial information in the representation coefficients of HSNRBs to improve denoising performances. Specifically, we employ low-rank subspace representation to exploit the global spectral correlation of HSI and transform the HSI denoising task as the estimation of spectral basis and spatial representation coefficients (SRCs). Motivated by the consistency of coefficient features between the whole HSI and HSNRBs, we employ the SRCs of HSNRBs to guide the restoration of target coefficients. To restore the SRCs accurately, we design a powerful nonlocal low-rank approximation that takes into account the nonlocal self-similarity (NSS) of SRCs. An efficient algorithm based on alternating minimization is developed to optimize the proposed model. Extensive experiments on both simulated and real-world data demonstrate the outperformance of our method.

1. Introduction

Hyperspectral image (HSI) is acquired by hyperspectral imaging sensors that are able to cover the wavelength region in the range of 0.4 to 2.5 μm. With abundant available spatial and spectral information, HSI has the potential to be superior in applications such as environmental monitoring [1], precision agriculture [2], military surveillance [3] and face recognition [4]. However, due to the instrumental noise, HSI is inescapably degraded by noise, which seriously destroys the data quality and limits the performance of subsequent applications. Therefore, HSI denoising has been regarded as an essential preprocessing step to improve image quality and downstream applications.

The existing HSI denoising methods can be roughly divided into two broad categories: deep learning-based approaches and model-based approaches [5]. Deep learning-based approaches design deep networks to learn the end-to-end mapping functions from the noisy HSI to the clean HSI [6–9]. This kind of method can deal with fast testing and achieve impressive restoration results, but requiring sufficient paired training data, training time, and calculation power. However, these networks suffer from the bottleneck of generalization ability in complicated noise

scenarios that are not included in the training data. Moreover, plenty of training data in the HSI community are hard to collect. On the contrary, model-based methods regard the task of HSI denoising as an ill-posed problem and introduce statistical priors such as smoothness [10–12], low-rank [13–17], and nonlocal self-similarity (NSS) [18–25], thus, improve good performance of deep learning-based in generalization and interpretable. However, most model-based approaches are dedicated to exploiting the complicated physical characteristics of HSI for boosting denoising performance, making the model complex and a heavy computational burden. Therefore, it should be a bottleneck for model-based methods to weaken the complex prior combination on this task, while improving their satisfactory restoration performance simultaneously. Moreover, most of them treat HSI as full-band noisy data and ignore an inconspicuous, but real phenomenon that there are many high signal-to-noise ratio bands (HSNRBs) in real HSI, which should be fully utilized to guide the denoising performance.

To handle the above bottlenecks, this article attempts to provide new insight into HSI denoising. Firstly, through empirical observation of real HSIs, we have found that not all bands of a captured HSI are

* Corresponding author.

E-mail addresses: chenyong1872008@163.com (Y. Chen), zj15070102719@163.com (J. Zhang), jinshanzeng@jxnu.edu.cn (J. Zeng), 202141600128@jxnu.edu.cn (W. Lai), xiaofeng@jxnu.edu.cn (X. Gui), taixiangjiang@gmail.com (T.-X. Jiang).

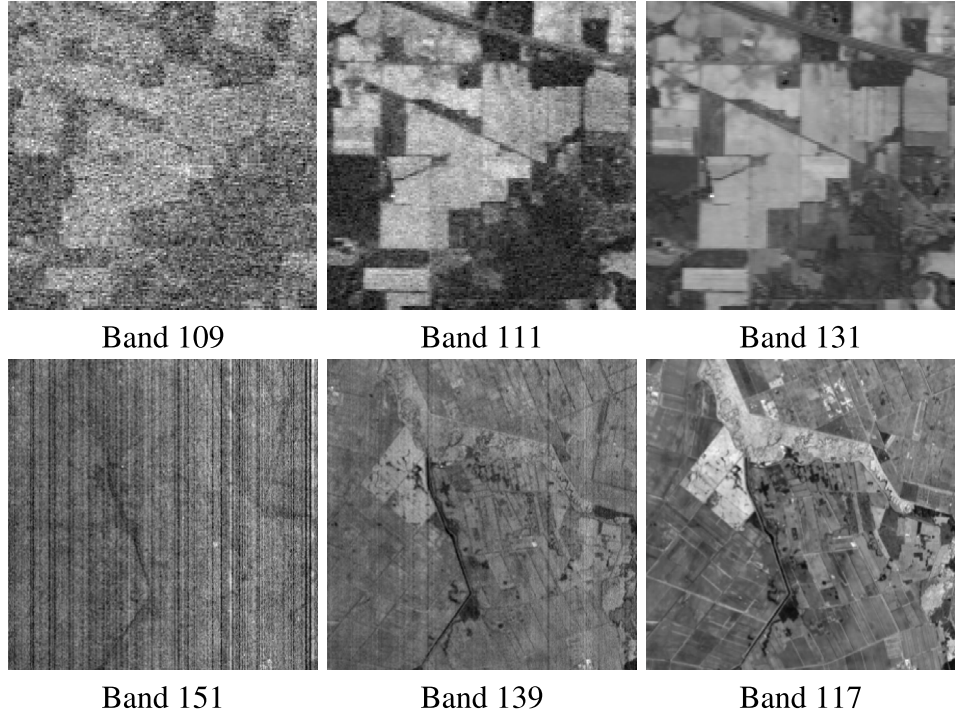


Fig. 1. The illustration of real-word HSIs with respect to different bands. Top: Indian Pines dataset. Bottom: GF-5 Baoqing dataset.

corrupted with noise, and there are many HSNRBs. Fig. 1 presents the illustration of different bands in the two real HSIs. Obviously, the levels of noise degradation are different in each band, and there are high-quality bands. This observation motivates us to investigate whether these HSNRBs can guide subsequent denoising. Secondly, it is known that the framework of subspace-based nonlocal low-rank approximation (SNLR) in model-based approaches has been extensively employed for HSI denoising with state-of-the-art results [23]. This kind of method first projects the original high-dimensional HSI onto a low-dimensional spectral subspace and then denoises the spatial representation coefficients (SRCs) via NSS methods. We extract two SRCs of the real GF-5 Baoqing dataset shown in Fig. 2(a)–(b). It is found that the SRCs are seriously degraded by noise, and the spatial information is largely invisible. Although spatial-based methods such as NSS can achieve effective SRCs restoration, many of them are heavily influenced by the type of noise, which reduces the accuracy of group matching and low-rank approximation. Thirdly, we can see that the SRCs of HSNRBs extracted from the GF-5 Baoqing dataset, as shown in Fig. 2(c), contain clear spatial information. Since SRCs inherit the spatial structure of the original HSI, and the spatial structure of HSNRBs is also consistent with those of the whole image, thus the SRCs of the whole HSI and those of HSNRBs also have the same spatial structure. This observation inspires us to investigate whether we can introduce this complementary information to guide the exact SRCs restoration of the entire noisy dataset. In conclusion, real noisy HSIs contain a significant number of HSNRBs, and making full use of this information without increasing the model complexity is a key factor in improving the performance of HSI denoising.

Based on the above observations, a novel method called Subspace-based Guided Nonlocal Low-Rank approximation (SGNLR) is proposed for HSI denoising. Unlike most model-based approaches that focus on utilizing complex priors of HSI, the SGNLR method proposes a new perspective by incorporating guidance information extracted from the noisy HSI. This approach does not increase the model complexity or its computational cost. By leveraging the guidance information, we integrate it into the powerful SNLR framework, which can effectively

preserve the spectral signature while better restoring the spatial structure. The flowchart of the proposed method is illustrated in Fig. 3. The main contributions of this paper are summarized as follows:

(1) We propose a novel perspective in the field of HSI denoising by incorporating guidance information from the noisy HSI. To the best of our knowledge, this is the first attempt to incorporate guidance information into nonlocal-based methods to improve their performance in this task.

(2) Based on the observation that the spatial structure of the HSNRBs exhibits similarities with the entire HSI, we incorporate this auxiliary information into an SNLR framework to guide the precise restoration of SRCs for the whole HSI.

(3) An efficient alternating minimization algorithm is designed to solve the proposed guided model. Experimental results on both simulated and real HSI datasets demonstrate that the proposed SGNLR method outperforms state-of-the-art nonlocal-based methods in terms of denoising performance.

The remainder of this paper is organized as follows. Section 2 briefly reviews the related work on HSI denoising. Some notations and problem formulation are presented in Section 3. Section 4 introduces the proposed SGNLR and its optimization procedure. A series of experiments with both simulated, real data and discussions are reported in Section 5. Finally, Section 6 concludes this paper.

2. Related work

This section briefly reviews the existing HSI denoising methods, which can be grouped into two categories: deep learning-based approaches and model-based approaches.

2.1. Deep learning-based approaches

Due to the powerful complex and high-representative feature learning capability of deep neural networks, deep learning-based approaches [26–30] have been widely applied in HSI processing. This kind of method implicitly learns the image prior from the paired training datasets and then performs a nonlinear end-to-end mapping between

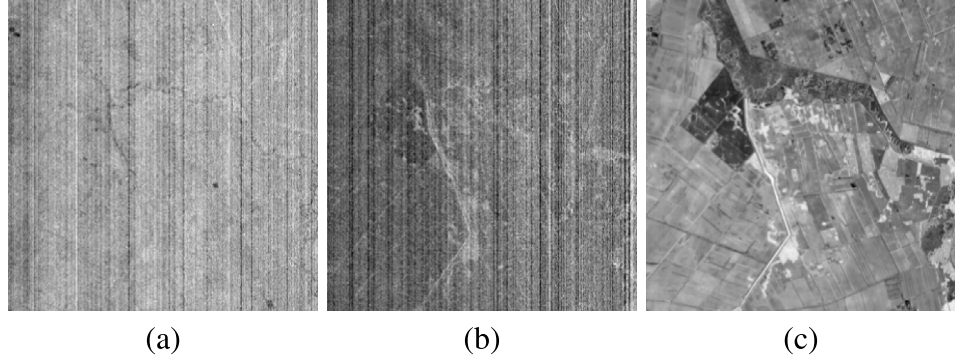


Fig. 2. The SRCs of the real GF-5 Baoqing dataset on the whole dataset and HSNRBs. (a)–(b) Two SRCs of the whole dataset. (c) One SRC of HSNRBs.

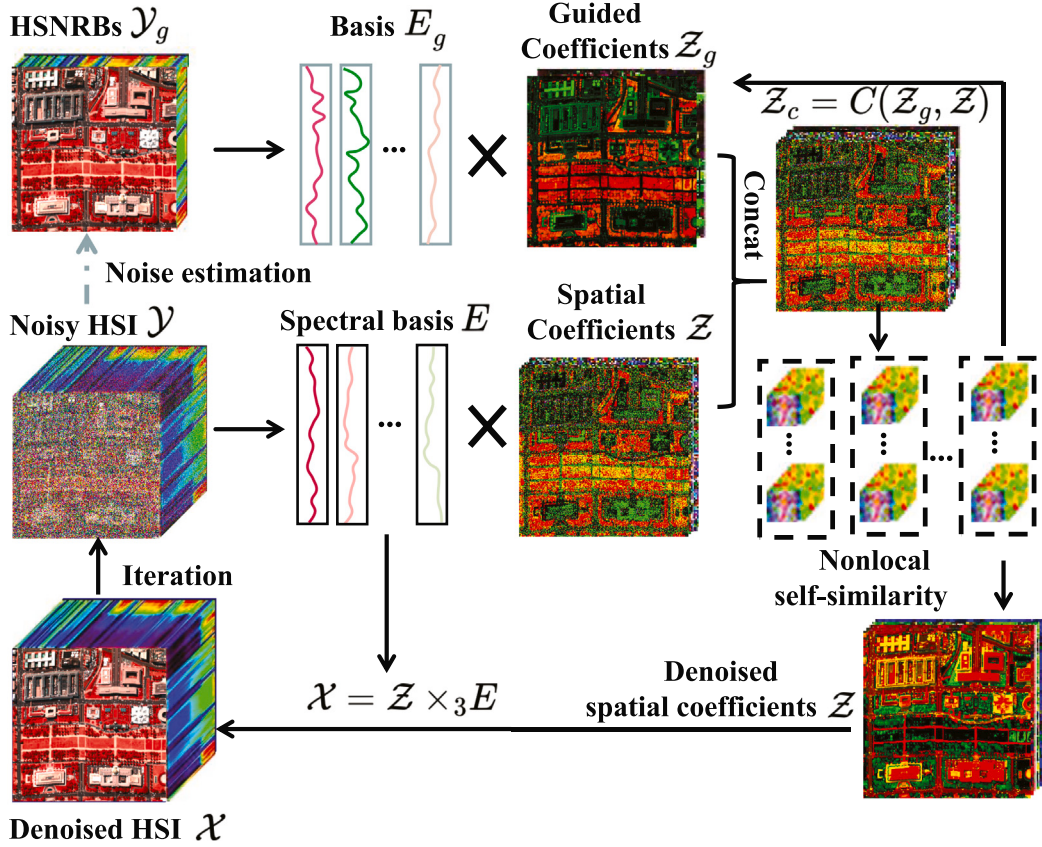


Fig. 3. Overall flowchart of the proposed SGNLR. First, low-rank subspace factorization is designed to capture the spectral correlation and reduce the computation complexity, which represents the HSI as the spectral basis and SRCs. Second, noise estimation is introduced to obtain the guided information (i.e., HSNRBs) from the noisy HSI. Third, the powerful NSS method is employed to denoise the spatial coefficients by incorporating the guided coefficients. Finally, iterative refinement is implemented to achieve the final result.

the noisy HSI and the clean HSI. Benefit from the effectiveness of convolutional neural networks (CNN) in natural image denoising, Chang et al. [7] first designed the CNN to learn a succession of 2-D convolutions for exploring the spatial structures of HSIs. To explore the spatial-spectral feature simultaneously, CNN-based derivatization methods were proposed for HSI denoising, such as spatial-spectral deep residual network [6] and spatial-spectral gradient network [31]. Since 2-D convolution-based CNNs cannot take full advantage of strong spectral correlation, a mount of works designed 3-D convolution to exploit

spatial-spectral correlations for HSI denoising, such as 3D U-net [8], 3-D-ADNet [32], and QRNN3D [26].

Although these CNN-based methods can obtain satisfactory results via training nonlinear mapping, the interpretability is relatively poor. To enhance the interpretability of CNN-based approaches for HSI denoising, T3SC [27] designed a spatial-spectral network by unraveling the iterative algorithm of a sparse coding model. SMDS-Net [33] proposed an end-to-end network by unfolding a subspace-based sparse model to simultaneously capture the spectral-spatial correlation and spatial sparsity priors. Give sufficient training data for different noise

types, deep learning-based methods are able to achieve better denoising results than the model-based counterparts. However, due to the complexity of noise distributions in real data, the trained networks may not be employed in others, while re-training a new network from scratch is impossible since the paired datasets are difficult to construct. In summary, these obstacles may limit the generalizability of deep learning-based methods.

2.2. Model-based approaches

Model-based approaches regard the task of HSI denoising as an ill-posed problem and develop an optimization model depicting the statistical priors of desired clean HSI. Three kinds of prior knowledge are generally employed in HSI denoising, including local smoothness, low-rank, and NSS.

The local smoothness is based on the fact that HSI has the sparse property under a specific dictionary or transform domain [34,35]. As the adjacent spatial areas and spectral bands have similar pixel values, total variation (TV) regularization is a powerful tool to characterize the local smoothness of HSI in the gradient domain and is widely employed for HSI denoising [10,16,36]. Moreover, the improved TV approaches are proposed to promote the performance of TV regularization for HSI denoising, such as enhanced 3D-TV regularization [37], spectral group TV regularization [38], and three-dimensional correlated total variation regularization [39]. The local smoothness prior is effective to preserve the spatial structure, but the spectral correlation is ignored.

Notice that the spectral correlation is induced by the fact that the spectral features of HSI are in a low-dimensional subspace. By unfolding the 3-D HSI into a 2-D matrix, matrix-based low-rank methods such as nuclear norm minimization [13], non-convex rank approximation [14, 15], and matrix factorization [12,34,40] are useful regularizations to capture the spectral correlation of HSI. Since the unfolding operator may destroy the original 3-D structure of HSI, tensor-based low-rank methods have been introduced to preserve the spatial-spectral correlation, including Tucker rank [41], CP rank [42,43], tubal rank [44,45], and tensor ring rank [46]. By integrating traditional/improved TV regularizations into the low-rank matrix/tensor framework priors, a large number of methods are proposed for HSI denoising, such as LRTV [11], LLRSSTV [47], LRTDTV [48]. Low-rank constraints on the spatial-spectral dimension can help restore the global information of HSI but still neglects an important intrinsic characteristic of NSS.

The NSS represents that they contain many similar full-band patches at different locations in the whole HSI. Representative examples of such methods in HSI denoising include tensor dictionary learning (TDL) [19], unidirectional low-rank tensor recovery (LLRT) [20], and Kronecker-basis-representation based tensor sparsity (KBR) [21]. The computational time of LLRT and KBR is relatively long due to the high dimensionality of the spectral band. To reduce the computational complexity, another improved method first projects the original high-dimensional HSI onto a low-dimensional spectral subspace and then denoises the SRCs via NSS methods [22,23,49,50]. For example, the fast hyperspectral denoising method (FastHyDe) [22] exploited the NSS of representation coefficients via block-matching and 3D filtering (BM3D), and nonlocal meets global method (NGmeet) [23] adopted weighted nuclear norm minimization (WNNM) to restore the similar full band patches. Although a satisfactory denoising result can be achieved by employing NSS methods, most of them treat HSI as full-band noisy data and ignore an inconspicuous but real phenomenon that there are many HSNRBs in real HSI, which should be fully utilized to guide the denoising performance.

3. Notations and problem formulation

3.1. Notations

In this article, lowercase letters or capital letters, lowercase bold letters, capitalized boldface letters, and capitalized calligraphic letters

are employed to represent scalars (e.g., k and K), vectors (e.g., \mathbf{x}), matrices (e.g., \mathbf{X}), and tensors (e.g., \mathcal{X}), respectively. For a N -order tensor $\mathcal{X} \in \mathbb{R}^{I_1 \times I_2 \times \dots \times I_N}$, the mode- n unfolding of \mathcal{X} is denoted by $\mathbf{X}_{(n)} \in \mathbb{R}^{I_n \times I_1 \times \dots \times I_{n-1} \times I_{n+1} \times \dots \times I_N}$. In contrast, we define $\text{fold}_n(\mathbf{X}_{(n)}) = \mathcal{X}$, where fold_n is the inverse operator of unfolding operator. The Frobenius norm of $\mathcal{X} \in \mathbb{R}^{I_1 \times I_2 \times \dots \times I_N}$ is defined by $\|\mathcal{X}\|_F = (\sum_{i_1} \sum_{i_2} \dots \sum_{i_N} x_{i_1 i_2 \dots i_N}^2)^{\frac{1}{2}}$. Moreover, the mode- n product of a tensor $\mathcal{X} \in \mathbb{R}^{I_1 \times I_2 \times \dots \times I_N}$ and a matrix $\mathbf{A} \in \mathbb{R}^{J_n \times I_n}$ is defined as $\mathcal{Y} = \mathcal{X} \times_n \mathbf{A}$, where $\mathcal{Y} \in \mathbb{R}^{I_1 \times \dots \times I_{n-1} \times J_n \times I_{n+1} \times \dots \times I_N}$ and $\mathcal{Y}_{i_1, \dots, i_{n-1}, j_n, i_{n+1}, \dots, i_N} = \sum_{i_n} \mathcal{X}_{i_1, \dots, i_N} \cdot \mathbf{A}_{j_n, i_n}$.

3.2. Degradation model

We consider $\mathcal{X} \in \mathbb{R}^{M \times N \times B}$ as a clean HSI with the spatial dimensions of $M \times N$ and B spectral bands. Under the contamination of additive zero-mean Gaussian noise, the observation model can be expressed as:

$$\mathcal{Y} = \mathcal{X} + \mathcal{N}, \quad (1)$$

where \mathcal{Y} is the observed HSI and \mathcal{N} is the additive Gaussian noise. HSI denoising is concerned with how to restore the underlying clean HSI \mathcal{X} from the observed noisy HSI \mathcal{Y} .

Generally, directly estimating the underlying HSI \mathcal{X} from the noisy HSI \mathcal{Y} is an ill-posed inverse problem. It is necessary to design regularization terms depicting the prior information of HSI for stable denoising. Motivated by the spectral correlation of HSI, low-rank prior is an effective tool to restore the HSI. However, as the spectral dimension increases, designing traditional low-rank approximation regularization, such as nuclear norm, to the original HSI is time-consuming. From the perspective of the linear mixing model, each spectral signature of HSI (i.e., the tube fiber of \mathcal{X}) can be formulated by a linear combination of a small number of pure spectral endmembers [51]. Thus, the HSI \mathcal{X} can be represented by

$$\mathcal{X} = \mathcal{Z} \times_3 \mathbf{E}, \quad (2)$$

where $\mathbf{E} \in \mathbb{R}^{B \times K}$ ($K \ll B$) is the endmember matrix and $\mathcal{Z} \in \mathbb{R}^{M \times N \times K}$ is the abundance coefficients. Mathematically, the variable \mathcal{X} has the low-rank property that can capture the spectral correlation of HSI. Specifically, we can also consider the expression in Eq. (2) as low-rank subspace decomposition, in which \mathbf{E} is a spectral basis matrix, and \mathcal{Z} is the SRCs. Based on the subspace decomposition, the observation model in Eq. (1) may be rewritten as:

$$\mathcal{Y} = \mathcal{Z} \times_3 \mathbf{E} + \mathcal{N}. \quad (3)$$

Therefore, the restoration of HSI is transformed as the estimation of spectral basis \mathbf{E} and SRCs \mathcal{Z} .

3.3. Subspace-based HSI denoising framework

By introducing the low-rank prior of HSI in the spectral dimension, the spectral basis \mathbf{E} and SRCs \mathcal{Z} can be alternately updated by the following regularization model:

$$\arg \min_{\mathcal{Z}, \mathbf{E}} \frac{1}{2} \|\mathcal{Y} - \mathcal{Z} \times_3 \mathbf{E}\|_F^2. \quad (4)$$

However, since the spatial prior is ignored, spectral low-rank prior alone cannot restore the spatial structure efficiently [23].

To improve the performance of Eq. (4), it is necessary to take into account the spatial prior of the original HSI. Since the original HSI \mathcal{X} is factorized into two factors, we cannot directly design the spatial prior to \mathcal{X} . Fortunately, with the orthogonal constraint of spectral basis matrix \mathbf{E} , the SRCs \mathcal{Z} maintain information of the original HSI \mathcal{X} [52]. The advantage of designing the spatial prior on the SRCs \mathcal{Z} is that it can reduce the complexity since the dimension of SRCs is much smaller than that of the original HSI. Incorporating the spatial prior of SRCs into Eq. (4), the denoising model can be rewritten as:

$$\arg \min_{\mathcal{Z}, \mathbf{E}} \frac{1}{2} \|\mathcal{Y} - \mathcal{Z} \times_3 \mathbf{E}\|_F^2 + \gamma R(\mathcal{Z}), \quad s.t. \mathbf{E}^T \mathbf{E} = \mathbf{I}, \quad (5)$$

where $R(\mathcal{Z})$ represents the regularization term characterizing the spatial prior of SRCs, and γ is the positive regularization parameter.

4. Proposed subspace-based guided nonlocal low-rank approximation method

As the SRCs inherit the spatial prior of the original HSI, spatial-based denoising regularizations can be employed to constrain the SRCs in the model Eq. (5), including TV regularization [11,52], BM3D denoiser [22], deep denoiser [53], and nonlocal self-similarity [23]. Among these spatial-based regularizations, the NSS which is depicted by low-rank performs excellent denoising results [54,55]. Moreover, the effective nonlocal low-rank approximation method with rigorous convergence theorems was first established in [56], which achieves state-of-the-art performances in model-based multiplicative noise removal. Therefore, the SNLR framework is formulated as:

$$\arg \min_{\mathcal{Z}, \mathbf{E}, \mathbf{G}_i} \frac{1}{2} \|\mathcal{Y} - \mathcal{Z} \times_3 \mathbf{E}\|_F^2 + \gamma \|\mathcal{Z}\|_{\text{NL}}, \quad \text{s.t. } \mathbf{E}^T \mathbf{E} = \mathbf{I}, \quad (6)$$

where $\|\mathcal{Z}\|_{\text{NL}} = \sum_i (\frac{1}{2} \|\mathcal{R}_i \mathcal{Z} - \mathbf{G}_i\|_F^2 + r(\mathbf{G}_i))$, \mathcal{R}_i is a operator extracting the i th exemplar patch group, \mathbf{G}_i is the low-rank component of $\mathcal{R}_i \mathcal{Z}$, and r is the low-rank approximation function.

4.1. The proposed SGNLR model

In this section, we present the proposed SGNLR model by incorporating the guided information into the SNLR framework in Eq. (6). The optimization of model in Eq. (6) can be alternatively updated by the following two subproblems:

$$\begin{cases} \mathbf{E} = \arg \min_{\mathbf{E}} \frac{1}{2} \|\mathcal{Y} - \mathcal{Z} \times_3 \mathbf{E}\|_F^2, \quad \text{s.t. } \mathbf{E}^T \mathbf{E} = \mathbf{I}, \\ \mathcal{Z} = \arg \min_{\mathcal{Z}} \frac{1}{2} \|\mathcal{Y} - \mathcal{Z} \times_3 \mathbf{E}\|_F^2 + \gamma \|\mathcal{Z}\|_{\text{NL}}. \end{cases} \quad (7)$$

With the SRCs \mathcal{Z} fixed, the optimization of \mathbf{E} -subproblem has the closed-form solution [14,23].

The solution to the \mathcal{Z} -subproblem consists of three steps: (1) searching for nonlocal groups $\mathcal{R}_i \mathcal{Z}$; (2) low-rank approximation $r(\cdot)$; (3) restoring the SRCs. The implementation of the first two steps directly impacts the restoration performance of SRCs. However, previous works have encountered two main issues. Firstly, these methods search for similar blocks directly on \mathcal{Z} , leading to inaccurate identification of similar blocks. This problem is exacerbated by the presence of irregular noises, which obscures spatial information. This issue is illustrated in Fig. 2(a)-(b). The SRCs contain significant irregular noise and lack spatial information, posing a significant challenge in the step of finding similar blocks, and ultimately affecting the subsequent steps. Secondly, due to the group matching operator, $\mathcal{R}_i \mathcal{Z}$ exhibits the low-rank property. Therefore, step 2 aims to extract the low-rank component from the noisy similar group. However, the inaccuracy of finding similar blocks in the first step, combined with the lack of information available in the SRCs, makes it challenging to achieve satisfactory results in the low-rank approximation step. This deficiency can negatively impact the performance of HSI denoising based on SNLR methods.

The main reason for these problems is that most of them treat HSI as full-band noisy data and ignore an inconspicuous but real phenomenon that there are many HSNRBs in real HSI. Fig. 1 presents three bands of two real datasets, and we can observe that some bands are heavily corrupted with noise, and some are apparently high-quality. Previous work has not extracted these bands separately, and how to make full use of them to improve the HSI denoising results is a key issue. To address the deficiencies of SNLR methods and improve its denoising ability, we propose a novel SGNLR model as follows:

$$\begin{aligned} \min_{\mathcal{Z}, \mathcal{Z}_g, \mathbf{G}_i} & \frac{1}{2} \|\mathcal{Y} - \mathcal{Z} \times_3 \mathbf{E}\|_F^2 + \frac{\beta}{2} \|\mathcal{Y}_g - \mathcal{Z}_g \times_3 \mathbf{E}_g\|_F^2 \\ & + \gamma \|\mathcal{Z}_c\|_{\text{NL}} \quad \text{s.t. } \mathbf{E}^T \mathbf{E} = \mathbf{I}, \end{aligned} \quad (8)$$

where \mathcal{Y}_g is the guided HSNRBs extracting from the noisy HSI \mathcal{Y} , \mathbf{E}_g and \mathcal{Z}_g are basis matrix and guided SRCs of HSNRBs, respectively. We definite $\mathcal{Z}_c = \mathcal{C}(\mathcal{Z}_g, \mathcal{Z})$ as the concatenation of two SRCs, and $\|\mathcal{Z}_c\|_{\text{NL}} = \sum_i (\frac{1}{2} \|\mathcal{R}_i \mathcal{Z}_c - \mathbf{G}_i\|_F^2 + r(\mathbf{G}_i))$ and $\mathbf{G}_i = [\mathbf{G}_{io}, \mathbf{G}_{ig}]$, where \mathbf{G}_{io}

and \mathbf{G}_{ig} are extracted from $\mathcal{R}_i \mathcal{Z}$ and $\mathcal{R}_i \mathcal{Z}_g$, respectively. Since HSNRBs are approximately clean data, we can learn the basis matrix \mathbf{E}_g from $\mathbf{Y}_{g,3}$ using singular value decomposition (SVD), where $\mathbf{Y}_{g,3}$ denotes the mode-3 unfolding of \mathcal{Y}_g .

Compared with the SNLR model in Eq. (6), the proposed SGNLR model has the following advantages. First, the SGNLR model can improve the precision of searching nonlocal patches. Although the SRCs of noisy images are of low quality, the SRCs of guided HSNRBs can provide high-quality spatial structure as shown in Fig. 2(c), which can be employed to guide the group matching. Second, the low-rank approximation of nonlocal groups will be more accurate on our SGNLR model. Since most of the spatial information from the noisy SRCs is corrupted, we can employ clean SRCs from HSNRBs to guide the low-rank approximation. This is analogous to low-rank completion, where the higher the observation ratio, the better the result [57]. Third, our SGNLR provides a new insight by introducing the guidance information, which does not increase the model complexity and its computational cost. Therefore, the proposed SGNLR model is expected to have a strong ability for noise removal.

4.2. Optimization

Due to the difficulty of optimizing multiple variables directly, the alternating minimization scheme is designed to solve the proposed SGNLR model in Eq. (8).

4.2.1. Spectral basis \mathbf{E} optimization

The subproblem of spectral basis \mathbf{E} optimization model in Eq. (8) is defined as:

$$\min_{\mathbf{E}} \frac{1}{2} \|\mathcal{Y} - \mathcal{Z} \times_3 \mathbf{E}\|_F^2, \quad \text{s.t. } \mathbf{E}^T \mathbf{E} = \mathbf{I}. \quad (9)$$

Actually, the closed-form solution of \mathbf{E} - subproblem is achieved by $\mathbf{E} = \mathbf{U} \mathbf{V}^T$, where \mathbf{U} and \mathbf{V} are the left and right singular vectors of $\mathbf{Y}_{(3)} \mathbf{Z}_{(3)}^T$, respectively. However, to preserve more detailed information, we employ iterative refinement during the iteration. Thus, we follow the strategy proposed in [23] to optimize it.

4.2.2. Low-rank approximation \mathbf{G}_i

Fixing other variables except \mathbf{G}_i , the subproblem of low-rank approximation \mathbf{G}_i is formulated as:

$$\min_{\mathbf{G}_i} \frac{1}{2} \|\mathcal{R}_i \mathcal{Z}_c - \mathbf{G}_i\|_F^2 + r(\mathbf{G}_i). \quad (10)$$

There are many denoising methods based on low-rank approximation, such as nuclear norm [11], Tucker decomposition [48], and intrinsic tensor sparsity regularization [21]. To balance the computation complexity and performance, we employ matrix-based WNNM [58] to estimate the low-rank component \mathbf{G}_i .

4.2.3. SRCs \mathcal{Z}_g update

Although the SRCs \mathcal{Z}_g is clean, we still need to iteratively update it in order to adaptively guide the restoration of the SRCs \mathcal{Z} and make these two SRCs promote each other. The objective function in Eq. (8) with respect to \mathcal{Z}_g is

$$\min_{\mathcal{Z}_g} \frac{\beta}{2} \|\mathcal{Y}_g - \mathcal{Z}_g \times_3 \mathbf{E}_g\|_F^2 + \gamma \sum_i \frac{1}{2} \|\mathcal{R}_i \mathcal{Z}_g - \mathbf{G}_{ig}\|_F^2. \quad (11)$$

By performing the inverse concatenation C^{-1} and discarding the constant term, the minimization problem is rewritten as:

$$\arg \min_{\mathcal{Z}_g} \frac{\beta}{2} \|\mathcal{Y}_g - \mathcal{Z}_g \times_3 \mathbf{E}_g\|_F^2 + \gamma \sum_i \frac{1}{2} \|\mathcal{R}_i \mathcal{Z}_g - \mathbf{G}_{ig}\|_F^2, \quad (12)$$

where \mathbf{G}_{ig} is the low-rank component corresponding to $\mathcal{R}_i \mathcal{Z}_g$. The \mathcal{Z}_g minimization is a quadratic optimization problem and can be solved by the following linear system:

$$(\gamma \sum_i \mathcal{R}_i^T \mathcal{R}_i + \beta \mathbf{I}) \mathbf{Z}_{g,3} = \beta \mathbf{E}_g^T \mathbf{Y}_{g,3} + \gamma \sum_i \mathcal{R}_i^T \mathbf{G}_{ig}, \quad (13)$$

where \mathcal{R}_i^T is the inverse operator of \mathcal{R}_i . Therefore, \mathcal{Z}_g is obtained by $\text{fold}_3(\mathbf{Z}_{g,3})$.

4.2.4. SRCs \mathcal{Z} restoration

Similar to the \mathcal{Z}_g -subproblem, the restoration of SRCs \mathcal{Z} is equivalent to solving the following minimization problem:

$$\arg \min_{\mathcal{Z}} \frac{\beta}{2} \|\mathcal{Y} - \mathcal{Z} \times_3 \mathbf{E}\|_F^2 + \gamma \sum_i \frac{1}{2} \|\mathcal{R}_i \mathcal{Z} - \mathbf{G}_{io}\|_F^2, \quad (14)$$

where \mathbf{G}_{io} is the low-rank component corresponding to $\mathcal{R}_i \mathcal{Z}$. The closed-form solution is obtained by solving the following linear system:

$$(\gamma \sum_i \mathcal{R}_i^T \mathcal{R}_i + \beta \mathbf{I}) \mathbf{Z}_{(3)} = \beta \mathbf{E}^T \mathbf{Y}_{(3)} + \gamma \sum_i \mathcal{R}_i^T \mathbf{G}_{io}. \quad (15)$$

Thus, we can obtain $\mathcal{Z} = \text{fold}_3(\mathbf{Z}_{(3)})$.

We summarize the solved algorithm for SGNLR model in Algorithm 1. To obtain the HSNRBs \mathcal{Y}_g , we first sketchy estimate the noise intensity of each band using a multiple regression theory-based method proposed in [51], and then extract the band whose noise intensity is less than a certain threshold value as the HSNRBs. We initialize these two SRCs as $\mathcal{Z} = \mathcal{Y} \times_3 \mathbf{E}^T$ and $\mathcal{Z}_g = \mathcal{Y}_g \times_3 \mathbf{E}_g^T$, where $\mathbf{E} = \mathbf{U}(:, 1 : K)$ and $\mathbf{E}_g = \mathbf{U}_g(:, 1 : c)$, \mathbf{U} and \mathbf{U}_g are the left singular matrices of $\mathbf{Y}_{(3)}$ and $\mathbf{Y}_{g,3}$, respectively. c is the number of features in the guided SRCs, and we set $c = 2$ to avoid the high computational complexity of nonlocal self-similarity. To compare fairness, we set $\mu = 2$ and $\delta = 0.1$ as suggested in [21,23].

5. Experimental results

In this section, we conduct both simulated and real experiments to verify the effectiveness of the proposed SGNLR method. We compare it against six state-of-the-art denoising approaches based on nonlocal methods, namely TDL [19], LLRT [20], KBR [21], FastHyDe [22], WLRTR [59], and NGmeet [23]. For all experiments, we manually adjust the parameters of these methods according to their default strategy or the rules described in their respective papers to obtain the best possible results. To facilitate numerical calculations and parameter adjustments, we normalize the pixel values of the entire HSI to the range of [0, 1] before conducting the experiments. All experiments are performed using MATLAB R2021b, running on an Intel(R) Core(TM) i7-7700 processor with 40 GB of RAM at 3.6 GHz.

Algorithm 1 SGNLR Solver

Input: Noisy HSI \mathcal{Y} , parameters β and γ .

1: **Initialize:** Global subspace dimension K , HSNRBs \mathcal{Y}_g , SRCs \mathcal{Z} and \mathcal{Z}_g .

2: **for** $t = 1 : \text{iter}$ **do**

3: Spectral basis \mathbf{E} learning via Eq. (9).

4: Low-rank approximation \mathbf{G}_i for all i via Eq. (10).

5: SRCs \mathcal{Z}_g update via Eq. (13).

6: SRCs \mathcal{Z} restoration via Eq. (15).

7: Dimension adaptation via $K \leftarrow \min(K + \mu * t, B)$.

8: Iterative update via $\mathcal{Y}^{(t)} \leftarrow \mathcal{Z} \times_3 \mathbf{E} + \delta(\mathcal{Y} - \mathcal{Z} \times_3 \mathbf{E})$.

9: **end for**

Output: The restored HSI $\mathcal{X} = \mathcal{Z} \times_3 \mathbf{E}$.

5.1. Simulated experiments

5.1.1. Experiments setting

We conduct simulated experiments using two publicly available HSI datasets: the Pavia City Center dataset (PaC), collected by the Reflection Optical System Imaging Spectrometer (ROSIS-03), and the Washington DC Mall (WDC) dataset, acquired by the Hyperspectral Digital Image Acquisition Experiment (HYDICE) sensor. Following previous works [60], we severally extract a sub-image of size $200 \times 200 \times 80$ for PaC and $256 \times 256 \times 191$ for WDC. To demonstrate the effectiveness of our new perspective in introducing guidance information, we follow the NGmeet method [23] and add Gaussian noise with zero-mean standard

variances 10, 30, 50, 100, and $U[30, 80]$, respectively. Moreover, to show that our method can be extended for complex noise removal, the mixtures of Gaussian noise, impulse noise, and stripe noise are added to the ground truth. The standard deviation of Gaussian noise and percentages of impulse noise is uniformly sampled within the range of $U[30, 80]$ and $U[0, 0.2]$, respectively. In addition, we select ten bands and thirty bands in PaC and WDC to add stripe noises, respectively. All parameters of the comparison methods were manually tuned to the optimum according to the authors' code or the recommendations in the paper. The two hyperparameters of our method are set to $\gamma = 10^{-1}$ and $\beta = 10^3$. The global subspace dimension K can be estimated by HySime [51]. Since many bands in the real data are high quality, we randomly select one-eighth of the bands without noise. It is worth noting that the test data for all methods is the same, i.e., one-eighth of the bands in the noisy data \mathcal{Y} are noise-free. Since most of the comparison methods are not pre-processed with noise, we also do not conduct noise preprocessing on FastHyDe for the sake of fairness in the comparison.

5.1.2. Quantitative comparison

To quantitatively evaluate the spatial and spectral restoration quality of the denoising results, three measures are chosen: peak signal-to-noise ratio (PSNR), structural similarity (SSIM), and spectral angle mapper (SAM). PSNR and SSIM are used to evaluate spatial quality, while SAM is a spectral-based index. Higher PSNR and SSIM values and lower SAM values indicate better restoration quality. Table 1 lists the quantitative results of all comparison methods under different noise levels on the PaC and WDC datasets. First, we can observe that the performance of subspace-based nonlocal methods is relatively better than that of global-based nonlocal approaches. The reason for this is that the global spectral and spatial correlations of HSI are effectively captured by low-rank subspace decomposition and nonlocal self-similarity, respectively. Second, the performance of TDL and NGmeet is dependent on the noise level, and they are relatively ineffective when the noise level is inconsistent in different bands. Third, we can easily observe that the proposed SGNLR achieves the best denoising performance in most noise cases. Another interesting observation is that although the proposed method is based on the framework of NGmeet, the performance of our SGNLR has significantly improved. This phenomenon confirms the effectiveness of our new insight by introducing guidance information in HSI processing.

5.1.3. Visual comparison

The previous quantitative comparison demonstrates the effectiveness of our SGNLR method. To provide a more intuitive comparison of denoising performance between different methods, we present visual comparisons to further illustrate the superiority of our method. Figs. 4 and 5 display the denoising and residual results of all comparison methods on PaC and WDC datasets, respectively. To facilitate visual comparison, we enlarge a patch of the restoration image in the lower left corner. It becomes apparent that TDL does not fully remove the noise, as evidenced by the visible noise in the enlarged box. Although LLRT and KBR perform better in removing noise, their excessive smoothing results in the removal of original image details. FastHyDe, WLRTR, NGmeet, and our proposed SGNLR method all effectively eliminate noise and retain image details, making it difficult to discern significant visual differences among them. To highlight the advantages of our approach, we present residual images that show the difference between the original image and the denoised result. The residual image demonstrates that our SGNLR method performs the best in minimizing residual artifacts, thereby effectively eliminating noise while preserving detailed information.

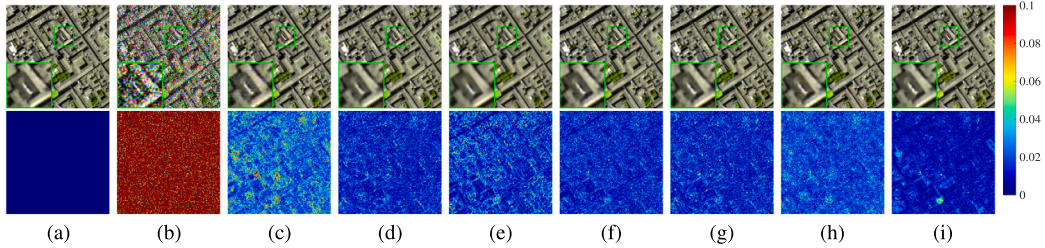


Fig. 4. Denoising and residual results of all comparison methods on the PaC dataset with bands 53-51-27 as R-G-B under noise level 50. (a) Original. (b) Noisy. (c) TDL. (d) LLRT. (e) KBR. (f) FastHyDe. (g) WLRTR. (h) NGmeet. (i) SGNLR.

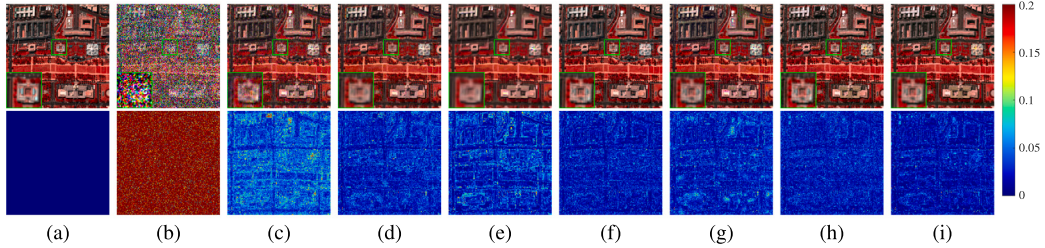


Fig. 5. Denoising and residual results of all comparison methods on the WDC dataset with bands 57-27-17 as R-G-B under noise level 100. (a) Original. (b) Noisy. (c) TDL. (d) LLRT. (e) KBR. (f) FastHyDe. (g) WLRTR. (h) NGmeet. (i) SGNLR.

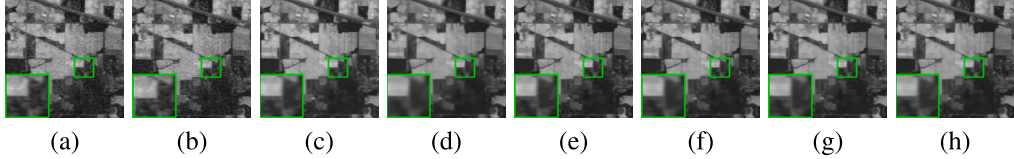


Fig. 6. Restoration results of all comparison methods on band 112 of the Indian Pines dataset. (a) Original. (b) TDL. (c) LLRT. (d) KBR. (e) FastHyDe. (f) WLRTR. (g) NGmeet. (h) SGNLR.

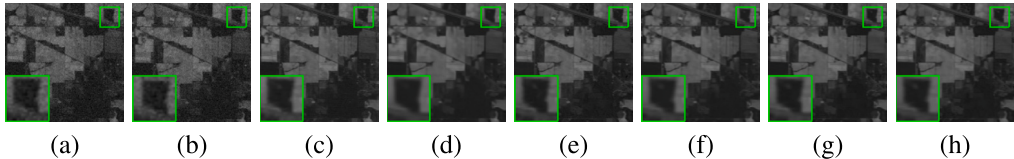


Fig. 7. Restoration results of all comparison methods on band 217 of the Indian Pines dataset. (a) Original. (b) TDL. (c) LLRT. (d) KBR. (e) FastHyDe. (f) WLRTR. (g) NGmeet. (h) SGNLR.

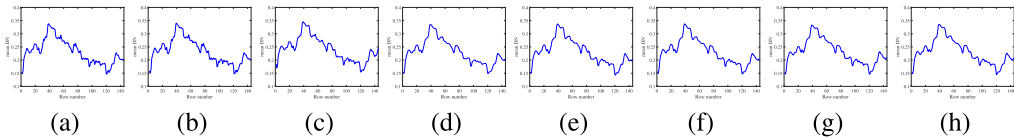


Fig. 8. Vertical mean DN profile of all comparison methods on band 217 of the Indian Pines dataset. (a) Original. (b) TDL. (c) LLRT. (d) KBR. (e) FastHyDe. (f) WLRTR. (g) NGmeet. (h) SGNLR.

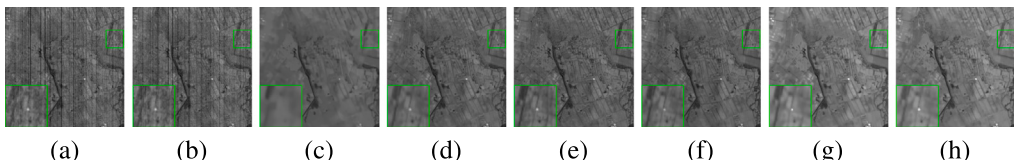


Fig. 9. Restoration results of all comparison methods on band 152 of the GF-5 Baoqing dataset. (a) Original. (b) TDL. (c) LLRT. (d) KBR. (e) FastHyDe. (f) WLRTR. (g) NGmeet. (h) SGNLR.

Table 1

Quantitative comparison of all comparison methods under different noise levels on the PaC and WDC datasets.

Cases	Index	Noisy	TDL	FastHyDe	KBR	LLRT	WLRTR	NGmeet	SGNLR
PaC	10	PSNR	28.13	33.72	42.53	40.36	42.29	41.60	42.70
		SSIM	0.801	0.922	0.991	0.985	0.990	0.989	0.991
		SAM	15.937	10.247	2.912	2.805	3.010	2.801	2.924
	30	PSNR	18.58	31.32	36.42	34.80	36.04	35.86	35.71
		SSIM	0.366	0.899	0.965	0.952	0.962	0.964	0.958
		SAM	34.970	9.910	4.787	4.223	5.360	4.581	6.124
	50	PSNR	14.15	28.82	33.78	31.74	33.39	33.15	32.83
		SSIM	0.188	0.836	0.941	0.908	0.938	0.936	0.925
		SAM	46.759	12.020	6.057	5.286	6.112	5.937	7.959
	100	PSNR	8.13	26.28	30.53	28.45	29.71	29.39	28.09
		SSIM	0.054	0.727	0.886	0.822	0.870	0.861	0.806
		SAM	63.380	13.711	7.817	6.759	7.177	8.617	12.824
	[30,80]	PSNR	13.74	25.59	33.15	30.84	31.41	30.57	27.90
		SSIM	0.194	0.677	0.933	0.889	0.893	0.876	0.784
		SAM	49.960	21.140	6.448	6.368	8.940	11.164	22.181
	Mixed	PSNR	12.17	21.32	24.51	23.35	17.04	16.31	23.44
		SSIM	0.128	0.526	0.800	0.664	0.307	0.280	0.759
		SAM	45.059	20.610	11.200	14.900	31.350	39.020	11.690
	10	PSNR	28.13	37.28	41.58	40.99	40.47	42.21	42.39
		SSIM	0.782	0.962	0.989	0.988	0.985	0.990	0.991
		SAM	16.244	6.132	3.842	2.863	4.210	3.029	3.326
	30	PSNR	18.59	30.08	37.49	35.12	35.16	37.00	37.90
		SSIM	0.372	0.852	0.973	0.956	0.953	0.970	0.976
		SAM	36.113	12.568	5.114	4.924	6.716	4.657	4.715
	50	PSNR	14.15	27.59	35.10	32.16	33.05	34.31	35.21
		SSIM	0.194	0.773	0.954	0.915	0.926	0.947	0.956
		SAM	48.83	15.229	6.123	6.186	7.471	5.915	5.949
	100	PSNR	8.13	24.82	31.84	28.69	29.68	29.53	31.44
		SSIM	0.059	0.639	0.909	0.819	0.851	0.855	0.904
		SAM	64.74	17.691	7.677	8.392	8.997	9.304	8.400
	[30,80]	PSNR	13.27	25.56	34.28	31.38	30.35	32.25	31.26
		SSIM	0.18	0.671	0.945	0.899	0.852	0.910	0.891
		SAM	52.047	20.973	6.484	6.919	11.130	8.267	12.398
	Mixed	PSNR	11.68	21.26	23.13	22.73	15.89	15.98	22.21
		SSIM	0.122	0.567	0.754	0.718	0.284	0.273	0.674
		SAM	47.370	20.670	15.460	15.970	37.350	41.580	15.960
									14.030

5.2. Real data experiments

In this section, we aim to further validate the effectiveness of our method in real data. To this end, we conduct experiments on two real HSIs: the AVIRIS Indian Pines dataset¹ and the GaoFen-5 Baoqing Dataset.² The AVIRIS Indian Pines dataset, acquired in 1992 by the Airborne Visible/Infrared Imaging Spectrometer sensor, comprises 220 spectral bands with a spatial size of 145×145 . The GF-5 Baoqing dataset, captured by the Hyperspectral GaoFen-5 satellite Collection, contains 210 bands. After removing the miss bands and extracting a small region. The GF-5 Baoqing sub-image with the size of $300 \times 300 \times 155$ is chosen for experiments. To extract the HSNRBs, we first estimate the noise level of each band using the multiple regression theory-based method and then select the top eighth of the bands with the lowest noise levels as the guidance data \mathcal{Y}_g . That is, the maximum value in the one-eighth band with the lowest noise levels is set as the threshold value.

Since the ground truth is not available for real datasets, objective evaluation metrics cannot be used to assess the effectiveness of different methods. Instead, we select two bands with moderate noise levels to compare the performance of different methods. Additionally, we plot the vertical (column) mean curve of one band to evaluate the denoising effect. Qualitative analysis of the denoising results and corresponding curves allows us to compare the effectiveness of different denoising methods.

5.2.1. Results on Indian pines dataset

Figs. 6 and 7 present the denoising results of all comparison methods on bands 112 and 217 of the Indian Pines dataset, respectively. From Figs. 6(a) and 7(a), we can find that this dataset is degraded by mixed Gaussian and impulse noise. The denoising results of LLRT and KBR are excessively smooth and lose a significant amount of detailed information. While the results obtained by FastHyDe effectively remove the noise, they still contain visible streaks. WLRTR, NGmeet, and our proposed SGNLR method outperform other competing methods by effectively removing noise while preserving more local details.

Fig. 8 shows the vertical mean profiles of the denoised image of band 217 in the Indian Pines dataset, where the horizontal and vertical axes denote the column number and the corresponding mean value of each column, respectively. It can be seen that TDL maintains the same curve as the noisy image, indicating that it fails to remove the noise. The results of LLRT and FastHyDe show some fluctuations due to the noise. Since KBR blurs the image detail, it obtains a smoother curve. On the other hand, WLRTR, NGmeet, and our proposed SGNLR achieve better results, showing neither fluctuations nor excessive smoothness.

5.2.2. Results on GF-5 Baoqing dataset

Figs. 9 and 10 present the bands 152 and 155 before and after denoising in the GF-5 Baoqing dataset. From Figs. 9 and 10(a), we can observe that this dataset is mainly degraded by Gaussian noise, impulse noise, and stripes. Apparently, TDL is not effective in removing noise in real experiments, which limits its application. Although LLRT can remove the noise completely, it results in the loss of spatial details. Compared with other methods, KBR can restore the image in a low-noise-intensity band, but there is still noise in the high-noise-intensity band. As shown in the enlarged box of Fig. 10(e)–(g), the denoised

¹ <https://engineering.purdue.edu/~biehl/MultiSpec/hyperspectral.html>

² <http://hipag.whu.edu.cn/resourcesdownload.html>

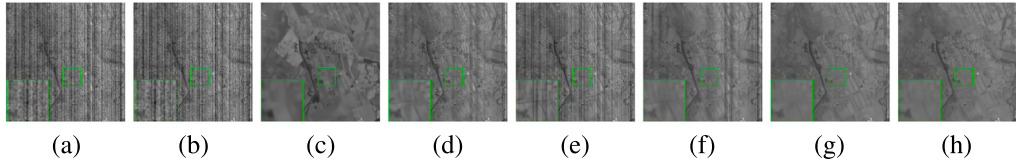


Fig. 10. Restoration results of all comparison methods on band 155 of the GF-5 Baoqing dataset. (a) Original. (b) TDL. (c) LLRT. (d) KBR. (e) FastHyDe. (f) WLRTR. (g) NGmeet. (h) SGNLR.

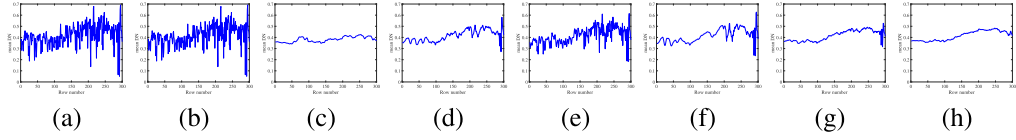


Fig. 11. Vertical mean DN profile of all comparison methods on band 155 of the GF-5 Baoqing dataset. (a) Original. (b) TDL. (c) LLRT. (d) KBR. (e) FastHyDe. (f) WLRTR. (g) NGmeet. (h) SGNLR.

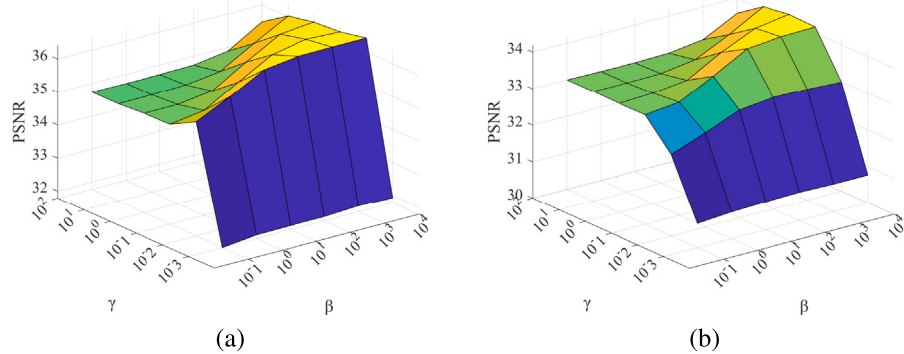


Fig. 12. Sensitivity analysis of parameters (β, γ) under two different noise levels. (a) Noise level 50. (b) Noise level [30, 80].

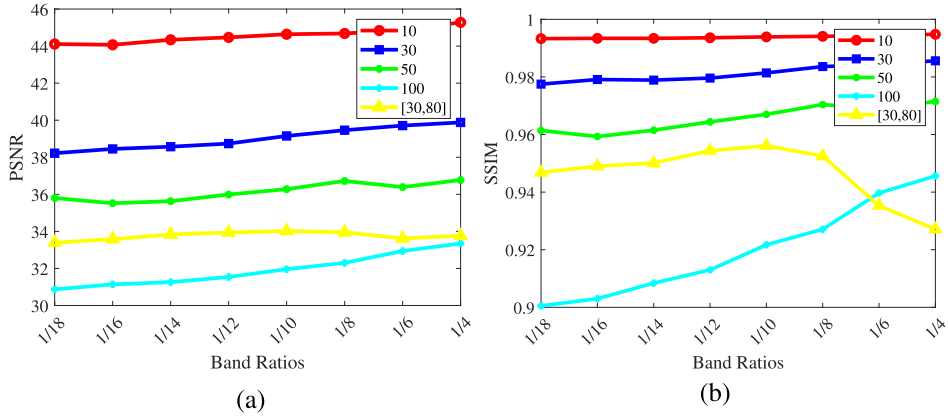


Fig. 13. Sensitivity analysis of the Number of HSNRBs under different noise levels. (a) PSNR. (b) SSIM.

results of FastHyDe, WLRTR, and NGmeet still have distinct stripes. The proposed method removes most of the noise and provides good denoised results. It is worth noting that our method has an advantage in detail recovery while ensuring that most of the noise is removed.

The vertical mean DN profiles of all comparison methods for band 155 are shown in Fig. 11. Except for TDL, all other methods diminish the fluctuations of the noisy image. LLRT and KBR achieve smoother curves, which can also be reflected in their visual results. FastHyDe can be seen to still have more pronounced fluctuations. Although WLRTR and NGmeet eliminate the apparent fluctuations, there are still some minor fluctuations. The result of our SGNLR is more reasonable than other methods. In summary, the experimental results on real

datasets once again demonstrate the effectiveness of our method and its competitiveness compared to other methods.

5.3. Discussion

In this section, we will discuss the parameter selection and convergence of the proposed method. Moreover, the sensitivity of the number of HSNRBs is analyzed. Furthermore, we present the time cost of all comparison methods on real datasets.

5.3.1. Parameter analysis

There are two regularization parameters in the SGNLR model that need to be selected in Algorithm 1: β and γ . We perform a sensitivity

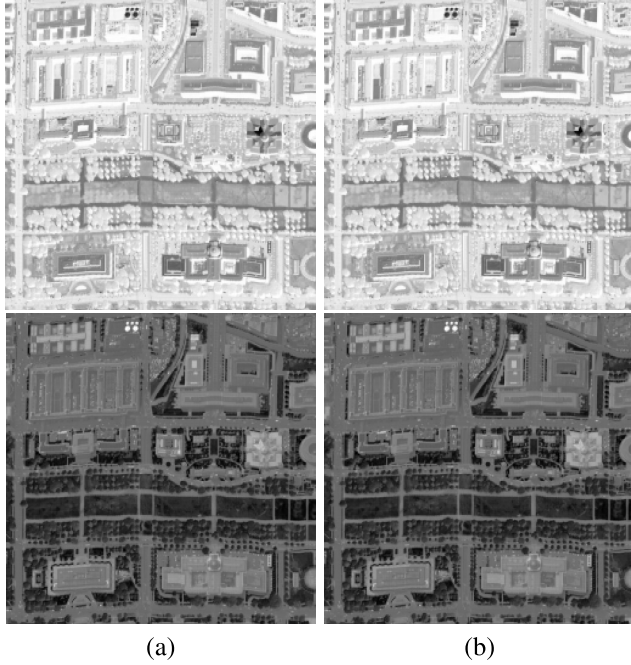


Fig. 14. The SRCs of HSNRBs before and after denoising. (a) Before denoising. (b) After denoising.

analysis on the simulated WDC dataset under noise levels of 50 and [30, 80]. Fig. 12 shows how the PSNR values change with the parameters β and γ . We find that the choice of parameters is relatively robust, as PSNR exhibits a consistent trend for parameter selection at different noise levels. Our SGNLR method performs relatively well when β and γ are in the range of $[10^3, 10^4]$ and $[10^{-2}, 10^{-1}]$, respectively. Therefore, we set $\beta = 10^3$ and $\gamma = 10^{-1}$ in all experiments.

5.3.2. The number of HSNRBs analysis

In our proposed method, HSNRBs are utilized to guide the restoration of SRCs. To evaluate the impact of the number of HSNRBs on the results, we vary the band ratio (the ratio of the guide band to the total spectral band) from the set of $[1/18, 1/16, 1/14, 1/12, 1/10, 1/8, 1/6, 1/4]$. Fig. 13 illustrates the PSNR and SSIM values for different band ratios on the simulated WDC dataset under varying noise levels. It can be observed that the restoration performance improves as the band ratio increases. Empirically, at least $1/8$ of the bands in real HSIs are high-quality, thus we select the $1/8$ bands with the least noise intensity as the HSNRBs. It is important to note that when all bands in HSIs are degraded by noise, our method will degrade to NGmeet.

To visually show the guided information, we compare the SRCs of HSNRBs before and after denoising on the simulated WDC dataset under noise level $U[30, 80]$ in Fig. 14. It is easy to see that the SRCs of HSNRBs have rich spatial information before and after denoising, and are basically consistent. This also confirms that these coefficients can guide the whole denoising process well.

5.3.3. Convergence analysis

Since the proposed SGNLR model in Eq. (8) is based on subspace decomposition, it is a nonconvex optimization problem. Therefore, it is difficult to theoretically guarantee convergence for nonconvex frameworks. We use numerical results to demonstrate the convergence. The PSNR and SSIM value curves with respect to the iteration number of the SGNLR solver are presented in Fig. 15. It can be seen that, after a few iterations, the PSNR and SSIM values remain stable for all noise cases, indicating the strong convergence of Algorithm 1.

5.3.4. Computational efficiency

The proposed method is based on the framework of NGmeet but does not introduce complex prior regularizations, so computational efficiency is guaranteed. Table 2 lists the time required for all the methods on real datasets. FastHyDe employs BM3D as the denoiser and does not iteratively update the spectral basis, so it is computationally inexpensive. LLRT, KBR, and WLRTR directly incorporate NSS into the original HSI design, resulting in high processing times. The proposed SGNLR is consistent with the time cost of NGmeet, but our method achieves significantly improved denoising results.

6. Conclusion

In this paper, we have provided a new perspective for HSI denoising. According to our observation, we observed a phenomenon that there are many HSNRBs in noisy HSI. By making full use of the guidance information in the HSNRBs, we proposed a new framework named SGNLR that can also simultaneously explore the global correlation and spatial NSS of HSI. As the SRCs of HSNRBs share the same spatial information as those of the clean HSI, we incorporated it into the SNLR approximation framework to guide HSI restoration. An efficient alternating minimization algorithm was used to solve the proposed model with a numerical convergence guarantee. Both simulated and real experiments verified the effectiveness of the proposed SGNLR method over some popular nonlocal-based methods. In the future, the new perspective of incorporating the HSNRBs can be extended to other HSI processing tasks. In addition, we can inject the complementary information of HSNRBs into the deep network to extract more refined spatial features so as to improve the performance of HSI denoising methods based on deep learning.

CRediT authorship contribution statement

Yong Chen: Conceptualization, Methodology, Validation, Writing – original draft, Writing – review & editing, Supervision, Funding acquisition. **Juan Zhang:** Formal analysis, Methodology, Software, Validation, Investigation, Writing – original draft, Visualization, Writing – review & editing. **Jinshan Zeng:** Methodology, Conceptualization, Writing – review & editing, Supervision, Funding acquisition. **Wenzen Lai:** Software, Validation, Investigation, Writing – review & editing. **Xinfeng Gui:** Software, Visualization, Writing – review & editing. **Tai-Xiang Jiang:** Validation, Writing – review & editing.

Declaration of competing interest

The authors declare that they have no known competing financial interests or personal relationships that could have appeared to influence the work reported in this paper.

Data availability

Data will be made available on request.

Acknowledgments

This work was supported in part by the National Natural Science Foundation of China under Grant 62101222, Grant 62376110, Grant 61977038, and Grant 12001446; in part by the Jiangxi Provincial Natural Science Foundation under Grant 20232ACB212001, Grant 20224BAB212001, and Grant 20224ACB212004, in part by the Thousand Talents Plan of Jiangxi Province under Grant jxsq2019201124, in part by the Natural Science Foundation of Sichuan, China under Grant 2022NSFSC1798, and in part by the Fundamental Research Funds for the Central Universities under Grant JBK2304066 and JBK2307052.

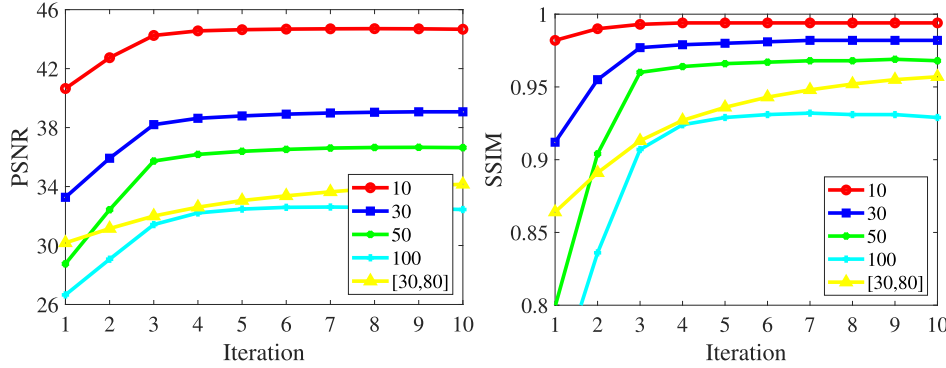


Fig. 15. PSNR and SSIM value curves in terms of the iteration number of SGNLR solver under different noise levels.

Table 2
Computational cost (in seconds) of all comparison methods on real datasets.

	TDL	LLRT	KBR	FastHyDe	WLRTR	NGmeet	SGNLR
Indian Pines	11.13	941.50	1908.71	0.11	1721.85	21.65	23.70
GF-5 Baoqing	47.34	2978.56	5037.03	0.54	4729.97	83.63	91.76

References

- [1] A. Plaza, J.A. Benediktsson, J.W. Boardman, J. Brazile, L. Bruzzone, G. Camps-Valls, J. Chanussot, M. Fauvel, P. Gamba, A. Gualtieri, et al., Recent advances in techniques for hyperspectral image processing, *Remote Sens. Environ.* 113 (2009) S110–S122.
- [2] H. Zhai, H. Zhang, P. Li, L. Zhang, Hyperspectral image clustering: Current achievements and future lines, *IEEE Geosc. Rem. Sens. M.* 9 (4) (2021) 35–67.
- [3] A.F. Goetz, Three decades of hyperspectral remote sensing of the earth: A personal view, *Remote Sens. Environ.* 113 (2009) S5–S16.
- [4] Z. Pan, G. Healey, M. Prasad, B. Tromberg, Face recognition in hyperspectral images, *IEEE Trans. Pattern Anal. Mach. Intell.* 25 (12) (2003) 1552–1560, <http://dx.doi.org/10.1109/TPAMI.2003.1251148>.
- [5] B. Rasti, Y. Chang, E. Dalsasso, L. Denis, P. Ghamisi, Image restoration for remote sensing: Overview and toolbox, *IEEE Geosci. Remote Sens. Mag.* (2021) 2–31, <http://dx.doi.org/10.1109/MGRS.2021.3121761>.
- [6] Q. Yuan, Q. Zhang, J. Li, H. Shen, L. Zhang, Hyperspectral image denoising employing a spatial-spectral deep residual convolutional neural network, *IEEE Trans. Geosci. Remote Sens.* 57 (2) (2018) 1205–1218.
- [7] Y. Chang, L. Yan, H. Fang, S. Zhong, W. Liao, HSI-DeNet: Hyperspectral image restoration via convolutional neural network, *IEEE Trans. Geosci. Remote Sens.* 57 (2) (2018) 667–682.
- [8] W. Dong, H. Wang, F. Wu, G. Shi, X. Li, Deep spatial-spectral representation learning for hyperspectral image denoising, *IEEE Trans. Comput. Imag.* 5 (4) (2019) 635–648.
- [9] X. Cao, X. Fu, C. Xu, D. Meng, Deep spatial-spectral global reasoning network for hyperspectral image denoising, *IEEE Trans. Geosci. Remote Sens.* 60 (2021) 1–14.
- [10] H.K. Aggarwal, A. Majumdar, Hyperspectral image denoising using spatio-spectral total variation, *IEEE Geosci. Remote Sens. Lett.* 13 (3) (2016) 442–446.
- [11] W. He, H. Zhang, L. Zhang, H. Shen, Total-variation-regularized low-rank matrix factorization for hyperspectral image restoration, *IEEE Trans. Geosci. Remote Sens.* 54 (1) (2016) 178–188.
- [12] Y. Chen, T.-Z. Huang, W. He, X.-L. Zhao, H. Zhang, J. Zeng, Hyperspectral image denoising using factor group sparsity-regularized nonconvex low-rank approximation, *IEEE Trans. Geosci. Remote Sens.* (2021) 1–16, <http://dx.doi.org/10.1109/TGRS.2021.3110769>.
- [13] H. Zhang, W. He, L. Zhang, H. Shen, Q. Yuan, Hyperspectral image restoration using low-rank matrix recovery, *IEEE Trans. Geosci. Remote Sens.* 52 (8) (2014) 4729–4743, <http://dx.doi.org/10.1109/TGRS.2013.2284280>.
- [14] Y. Xie, Y. Qu, D. Tao, W. Wu, Q. Yuan, W. Zhang, Hyperspectral image restoration via iteratively regularized weighted schatten p -norm minimization, *IEEE Trans. Geosci. Remote Sens.* 54 (8) (2016) 4642–4659.
- [15] Y. Chen, Y. Guo, Y. Wang, D. Wang, C. Peng, G. He, Denoising of hyperspectral images using nonconvex low rank matrix approximation, *IEEE Trans. Geosci. Remote Sens.* 55 (9) (2017) 5366–5380.
- [16] S. Xu, J. Zhang, C. Zhang, Hyperspectral image denoising by low-rank models with hyper-Laplacian total variation prior, *Signal Process.* 201 (2022) 108733.
- [17] Z. Tu, J. Lu, H. Zhu, H. Pan, W. Hu, Q. Jiang, Z. Lu, A new nonconvex low-rank tensor approximation method with applications to hyperspectral images denoising, *Inverse Problems* 39 (6) (2023) 065003.
- [18] M. Maggioni, V. Katkovnik, K. Egiazarian, A. Foi, Nonlocal transform-domain filter for volumetric data denoising and reconstruction, *IEEE Trans. Image Process.* 22 (1) (2013) 119–133.
- [19] Y. Peng, D. Meng, Z. Xu, C. Gao, Y. Yang, B. Zhang, Decomposable nonlocal tensor dictionary learning for multispectral image denoising, in: 2014 IEEE Conference on Computer Vision and Pattern Recognition, 2014, pp. 2949–2956, <http://dx.doi.org/10.1109/CVPR.2014.377>.
- [20] Y. Chang, L. Yan, S. Zhong, Hyper-laplacian regularized unidirectional low-rank tensor recovery for multispectral image denoising, in: IEEE Conf. Comput. Vis. Pattern Recog., 2017, pp. 4260–4268.
- [21] Q. Xie, Q. Zhao, D. Meng, Z. Xu, Kronecker-basis-representation based tensor sparsity and its applications to tensor recovery, *IEEE Trans. Pattern Anal. Mach. Intell.* 40 (8) (2018) 1888–1902.
- [22] L. Zhuang, J.M. Bioucas-Dias, Fast hyperspectral image denoising and inpainting based on low-rank and sparse representations, *IEEE J. Sel. Topics Appl. Earth Observ. Remote Sens.* 11 (3) (2018) 730–742.
- [23] W. He, Q. Yao, C. Li, N. Yokoya, Q. Zhao, H. Zhang, L. Zhang, Non-local meets global: An integrated paradigm for hyperspectral image restoration, *IEEE Trans. Pattern Anal. Mach. Intell.* (2020) 1–18, <http://dx.doi.org/10.1109/TPAMI.2020.3027563>.
- [24] J. Xue, Y. Zhao, W. Liao, J.C.-W. Chan, Nonlocal low-rank regularized tensor decomposition for hyperspectral image denoising, *IEEE Trans. Geosci. Remote Sens.* 57 (7) (2019) 5174–5189.
- [25] C. He, L. Sun, W. Huang, J. Zhang, Y. Zheng, B. Jeon, TSLRLN: Tensor subspace low-rank learning with non-local prior for hyperspectral image mixed denoising, *Signal Process.* 184 (2021) 108060.
- [26] K. Wei, Y. Fu, H. Huang, 3-d quasi-recurrent neural network for hyperspectral image denoising, *IEEE Trans. Neural Netw. Learn. Syst.* 32 (1) (2020) 363–375.
- [27] T. Bodroto, A. Zouaoui, J. Chanussot, J. Mairal, A trainable spectral-spatial sparse coding model for hyperspectral image restoration, in: Adv. Neural. Inf. Process. Syst. vol. 34, 2021, pp. 5430–5442.
- [28] R. Dian, A. Guo, S. Li, Zero-shot hyperspectral sharpening, *IEEE Trans. Pattern Anal. Mach. Intell.* (2023) 1–17, <http://dx.doi.org/10.1109/TPAMI.2023.3279050>.
- [29] R. Dian, T. Shan, W. He, H. Liu, Spectral super-resolution via model-guided cross-fusion network, *IEEE Trans. Neural Netw. Learn. Syst.* (2023) 1–12, <http://dx.doi.org/10.1109/TNNLS.2023.3238506>.
- [30] Y. Chen, X. Gui, J. Zeng, X.-L. Zhao, W. He, Combining low-rank and deep plug-and-play priors for snapshot compressive imaging, *IEEE Trans. Neural Netw. Learn. Syst.* (2023) 1–13, <http://dx.doi.org/10.1109/TNNLS.2023.3294262>.
- [31] Q. Zhang, Q. Yuan, J. Li, X. Liu, H. Shen, L. Zhang, Hybrid noise removal in hyperspectral imagery with a spatial-spectral gradient network, *IEEE Trans. Geosci. Remote Sens.* 57 (10) (2019) 7317–7329.
- [32] Q. Shi, X. Tang, T. Yang, R. Liu, L. Zhang, Hyperspectral image denoising using a 3-D attention denoising network, *IEEE Trans. Geosci. Remote Sens.* 59 (12) (2021) 10348–10363.
- [33] F. Xiong, J. Zhou, S. Tao, J. Lu, J. Zhou, Y. Qian, SMDS-net: Model guided spectral-spatial network for hyperspectral image denoising, *IEEE Trans. Image Process.* 31 (2022) 5469–5483.
- [34] Y.Q. Zhao, J. Yang, Hyperspectral image denoising via sparse representation and low-rank constraint, *IEEE Trans. Geosci. Remote Sens.* 53 (1) (2015) 296–308.
- [35] Y. Chen, W. He, X.-L. Zhao, T.-Z. Huang, J. Zeng, H. Lin, Exploring nonlocal group sparsity under transform learning for hyperspectral image denoising, *IEEE Trans. Geosci. Remote Sens.* 60 (2022) 1–18.

- [36] Q. Yuan, L. Zhang, H. Shen, Hyperspectral image denoising employing a spectral-spatial adaptive total variation model, *IEEE Trans. Geosci. Remote Sens.* 50 (10) (2012) 3660–3677.
- [37] J. Peng, Q. Xie, Q. Zhao, Y. Wang, L. Yee, D. Meng, Enhanced 3DTV regularization and its applications on HSI denoising and compressed sensing, *IEEE Trans. Image Process.* 29 (2020) 7889–7903, <http://dx.doi.org/10.1109/TIP.2020.3007840>.
- [38] Y. Chen, W. He, N. Yokoya, T.-Z. Huang, Hyperspectral image restoration using weighted group sparsity-regularized low-rank tensor decomposition, *IEEE Trans. Cybern.* 50 (8) (2020) 3556–3570.
- [39] J. Peng, Y. Wang, H. Zhang, J. Wang, D. Meng, Exact decomposition of joint low rankness and local smoothness plus sparse matrices, *IEEE Trans. Pattern Anal. Mach. Intell.* (2022) 1–16, <http://dx.doi.org/10.1109/TPAMI.2022.3204203>.
- [40] Y. Chen, X. Cao, Q. Zhao, D. Meng, Z. Xu, Denoising hyperspectral image with non-iid noise structure, *IEEE Trans. Cybern.* 48 (3) (2018) 1054–1066.
- [41] A. Karami, M. Yazdi, A.Z. Asli, Noise reduction of hyperspectral images using kernel non-negative tucker decomposition, *IEEE J. Sel. Top. Signal. Process.* 5 (3) (2011) 487–493.
- [42] X. Liu, S. Bourennane, C. Fossati, Denoising of hyperspectral images using the PARAFAC model and statistical performance analysis, *IEEE Trans. Geosci. Remote Sens.* 50 (10) (2012) 3717–3724.
- [43] X. Guo, X. Huang, L. Zhang, Hyperspectral image noise reduction based on rank-1 tensor decomposition, *ISPRS J. Photogramm. Remote Sens.* 83 (2013) 50–63.
- [44] H. Fan, Y. Chen, Y. Guo, H. Zhang, G. Kuang, Hyperspectral image restoration using low-rank tensor recovery, *IEEE J. Sel. Topics Appl. Earth Observ. Remote Sens.* 10 (10) (2017) 4589–4604.
- [45] Y.-B. Zheng, T.-Z. Huang, X.-L. Zhao, T.-X. Jiang, T.-H. Ma, T.-Y. Ji, Mixed noise removal in hyperspectral image via low-fibered-rank regularization, *IEEE Trans. Geosci. Remote Sens.* 58 (1) (2020) 734–749.
- [46] Y. Chen, J. Zeng, W. He, X.-L. Zhao, T.-Z. Huang, Hyperspectral and multispectral image fusion using factor smoothed tensor ring decomposition, *IEEE Trans. Geosci. Remote Sens.* 60 (2022) 1–17.
- [47] W. He, H. Zhang, H. Shen, L. Zhang, Hyperspectral image denoising using local low-rank matrix recovery and global spatial-spectral total variation, *IEEE J. Sel. Topics Appl. Earth Observ. Remote Sens.* 11 (3) (2018) 713–729.
- [48] Y. Wang, J. Peng, Q. Zhao, Y. Leung, X.-L. Zhao, D. Meng, Hyperspectral image restoration via total variation regularized low-rank tensor decomposition, *IEEE J. Sel. Topics Appl. Earth Observ. Remote Sens.* 11 (4) (2018) 1227–1243.
- [49] T.-X. Jiang, L. Zhuang, T.-Z. Huang, X.-L. Zhao, J.M. Bioucas-Dias, Adaptive hyperspectral mixed noise removal, *IEEE Trans. Geosci. Remote Sens.* 60 (2022) 1–13, <http://dx.doi.org/10.1109/TGRS.2021.3085779>.
- [50] L. Zhuang, X. Fu, M.K. Ng, J.M. Bioucas-Dias, Hyperspectral image denoising based on global and nonlocal low-rank factorizations, *IEEE Trans. Geosci. Remote Sens.* 59 (12) (2021) 10438–10454, <http://dx.doi.org/10.1109/TGRS.2020.3046038>.
- [51] J.M. Bioucas-Dias, J.M. Nascimento, Hyperspectral subspace identification, *IEEE Trans. Geosci. Remote Sens.* 46 (8) (2008) 2435–2445.
- [52] J. Peng, H. Wang, X. Cao, X. Liu, X. Rui, D. Meng, Fast noise removal in hyperspectral images via representative coefficient total variation, *IEEE Trans. Geosci. Remote Sens.* 60 (2022) 1–17.
- [53] Y.-C. Miao, X.-L. Zhao, X. Fu, J.-L. Wang, Y.-B. Zheng, Hyperspectral denoising using unsupervised disentangled spatirospectral deep priors, *IEEE Trans. Geosci. Remote Sens.* 60 (2021) 1–16.
- [54] R. Dian, S. Li, L. Fang, T. Lu, J.M. Bioucas-Dias, Nonlocal sparse tensor factorization for semiblind hyperspectral and multispectral image fusion, *IEEE Trans. Cybern.* 50 (10) (2020) 4469–4480, <http://dx.doi.org/10.1109/TCYB.2019.2951572>.
- [55] J. Lu, C. Xu, Z. Hu, X. Liu, Q. Jiang, D. Meng, Z. Lin, A new nonlocal low-rank regularization method with applications to magnetic resonance image denoising, *Inverse Problems* 38 (6) (2022) 065012.
- [56] X. Liu, J. Lu, L. Shen, C. Xu, Y. Xu, Multiplicative noise removal: nonlocal low-rank model and its proximal alternating reweighted minimization algorithm, *SIAM J. Imaging Sci.* 13 (3) (2020) 1595–1629.
- [57] F.J. Király, L. Theran, R. Tomioka, The algebraic combinatorial approach for low-rank matrix completion, *J. Mach. Learn. Res.* 16 (1) (2015) 1391–1436.
- [58] S. Gu, L. Zhang, W. Zuo, X. Feng, Weighted nuclear norm minimization with application to image denoising, in: *IEEE Conf. Comput. Vis. Pattern Recog.*, 2014, pp. 2862–2869.
- [59] Y. Chang, L. Yan, X.-L. Zhao, H. Fang, Z. Zhang, S. Zhong, Weighted low-rank tensor recovery for hyperspectral image restoration, *IEEE Trans. Cybern.* 50 (11) (2020) 4558–4572.
- [60] S. Xu, X. Cao, J. Peng, Q. Ke, C. Ma, D. Meng, Hyperspectral image denoising by asymmetric noise modeling, *IEEE Trans. Geosci. Remote Sens.* 60 (2022) 1–14.